Available online at www.sciencedirect.com

ScienceDirect

journal homepage: www.elsevier.com/locate/he

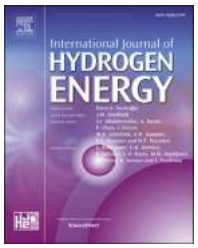

The effect of baffle shape on the performance of a polymer electrolyte membrane fuel cell with a biometric flow field

Arasy Fahruddin [a,1,*], *Djatmiko Ichsani* [a], *Fadlilatul Taufany* [b,**], *Budi U.K. Widodo* [a], *Wawan A. Widodo* [a]

[a] *Department of Mechanical Engineering, Institut Teknologi Sepuluh Nopember (ITS), Jl. Raya ITS, Surabaya, 60111, Jawa Timur, Indonesia*

[b] *Department of Chemical Engineering, Institut Teknologi Sepuluh Nopember (ITS), Jl. Raya ITS, Surabaya, 60111, Jawa Timur, Indonesia*

HIGHLIGHTS

- Adding baffles will increase the uniformity of the reactant distribution.
- The uniformity of Oxygen distribution is proportional to current density.
- Baffles will prevent the reactants from flowing directly to the outlet.
- The use of rectangular baffles in mother channel produces better performance.

ARTICLE INFO

Article history:
Received 6 February 2020
Received in revised form
1 July 2020
Accepted 6 August 2020
Available online 30 August 2020

Keywords:
Baffle shape
Leaf flow field
Polymer electrolyte membrane fuel cell

ABSTRACT

Flow field design on the cathode side, inspired by leaf shapes, leads to a high performance, as it achieves a good distribution of reactants. Furthermore, the addition of baffles to the cathode channel also increases the supply of reactants in the cathode catalyst. However, research on the addition of baffles to the cathode channel has still been limited to straight channels and conventional flow fields. Therefore, in this work, a numerical study was conducted to investigate the effect of baffles on the leaf flow field on the performance of a polymer electrolyte membrane fuel cell. The generated 3D model is composed of nine layers with a 25-cm^2 active area. The beam and chevron shapes of the baffles, which were inserted into the mother channel, were compared. The simulation results revealed that the addition of beam-shaped baffles that are close to each other can increase the current and power densities by up to 18% due to the more uniform distribution of the oxygen mass fraction.

* *Corresponding author.*
** *Corresponding author.*
E-mail addresses: arasy.fahruddin@umsida.ac.id (A. Fahruddin), f_taufany@chem-eng.its.ac.id (F. Taufany).
[1] Working in the Department of Mechanical Engineering, Universitas Muhammadiyah Sidoarjo (Umsida), Sidoarjo, Indonesia. Conducting this research while studying in the Department of Mechanical Engineering, Institut Teknologi Sepuluh Nopember (ITS), Surabaya, Indonesia.

https://doi.org/10.1016/j.ijhydene.2020.08.054

Introduction

The fuel cell is an energy conversion engine that converts the internal energy of the fuel directly into electricity [1,2], thus resulting in minimal heat and mechanical losses. Furthermore, fuel cells require less refueling time and lower weight and storage volume. In a previous study, approximately half of the weight and volume were required, when compared with commonly used batteries, for the vehicle to reach a 500-km distance [3]. In particular, the hydrogen fuel cell is more environmentally friendly, as only water vapor is produced as a residue [4]. In addition, hydrogen is a renewable energy source, as it can be produced by electrolysis [5]. Meanwhile, the polymer electrolyte membrane fuel cell (PEMFC) is more suitable for mobile applications owing to its high efficiency at relatively low temperatures [6,7]. Fuel cells, however, are still relatively expensive compared with other energy conversion engines.

As a result, researchers have conducted studies to achieve higher power density in fuel cells. Moreover, a higher power density would lead to more compact cells, benefiting mobile applications [6]. One important factor influencing power density is the geometry where the flow is located, which can increase the power density by up to 50% [8–11]. The design of this geometry affects the supply of fuel to the catalyst, where the electrochemical reaction occurs [12,13]. A study conducted by Roshandel et al. (2012) indicated that geometries inspired by leaf shapes resulted in an increase of up to 26% in power density compared with the conventional shape [14]. Meanwhile, Kloess et al. (2009) and Guo et al. (2014) have examined the interdigitated leaf design, and their results revealed an increase in PEMFC performance between 25% and 30% when compared with conventional designs [15,16]. However, the mechanism of drainage and the large pressure drop on the cathode side for interdigitation design were not analyzed in detail. Ozden et al. (2017) compared the results of the three designs of bio-inspired flow geometries and triple serpentine combined with various configurations on the anode and cathode sides in a direct methanol fuel cell. The results revealed that the combination of the serpentine geometry on the anode side and the leaf flow field on the cathode side resulted in the best performance [17]. In this study, we adapted the second bio-inspired leaf flow field configuration proposed by Ozden with the channel dimensions used in our previous research [18,19].

Furthermore, Heidary et al. (2016) examined the addition of baffles to parallel flow fields and demonstrated that their presence in the channel would significantly increase power density [20,21]. Other researchers have also revealed an increase in PEM fuel cell performance owing to the addition of baffles and other types of blockage to the channel [22–25]. From these previous studies, the combination of leaf geometry and the addition of baffles to each channel would lead to a further increase in power density; therefore, the performance of this configuration should be investigated.

The leaf-shaped geometry is composed of mother and daughter channels in the form of a branch. The mother channel connects the supplier to the branches; therefore, adding baffles to this channel would affect the distribution of reactants near the inlet area to the outlet area. As a result, this study discussed the effects of the shape and arrangement of the baffles in the mother channel on the performance of the fuel cell.

Materials and methods

Model assumption and boundary condition

The 3D model used in this work consisted of nine parts: a pair of current collectors, fluids, gas diffusion layers, catalyst layers, and a membrane. The model had a 25-cm^2 active area [26]. Moreover, the geometry of the anode was a single serpentine which was 1-mm thick and wide, whereas that of the cathode side was a leaf-inspired design with baffles in the mother channel and daughter channels. The depth and width of the daughter channel were 1 mm [19]. The shape and arrangement of the baffles on the mother channel varied, as presented in Fig. 1. Meanwhile, the baffles on the daughter channel were square, with a height of 0.5 mm, which allowed a medium pressure drop [21,23] and a better flow distribution to each branch due to the tendency of the flow toward lower resistance [27]. Moreover, they were arranged as presented in Fig. 2. The generated model was, thereafter, meshed, and the boundary and operation conditions were inputted afterward based on the data presented in Table 1.

The following assumptions have been applied in the PEMFC model calculation:

1. PEMFC works in steady conditions.
2. Gravitational effects were not included.
3. Laminar flow in the gas channel (low Reynolds number).
4. Isotropic and homogeneous porous media.
5. The Butler–Volmer equation was applied to solve the electrochemical reaction in the catalyst layer.

Governing equations

The governing conservation equation, which could be applied to different quantities, ϕ (mass, energy, and transport of species), was defined as [20]:

$$\nabla.\left(\rho\phi\overrightarrow{V}\right) = \nabla.\left(\Gamma_{\phi}\nabla\phi\right) + S_{\phi} \quad (1)$$

where ρ denotes the density of the mixture; $\overrightarrow{V}$, the velocity vector; Γ_{ϕ}, the diffusion of the quantity; and S_{ϕ}, the source term. The first and second terms represent the transportation due to convection and diffusion, respectively. Meanwhile, the third one is the source term, which could not be included in the previous term, such as heat generation.

The Butler–Volmer equation, which is a default equation on the Ansys–Fluent software [29], was used to calculate the transfer current inside the catalyst layer. The electrical current at the anode (R_a) and cathode (R_c) sides, was, therefore, calculated using the following equations:

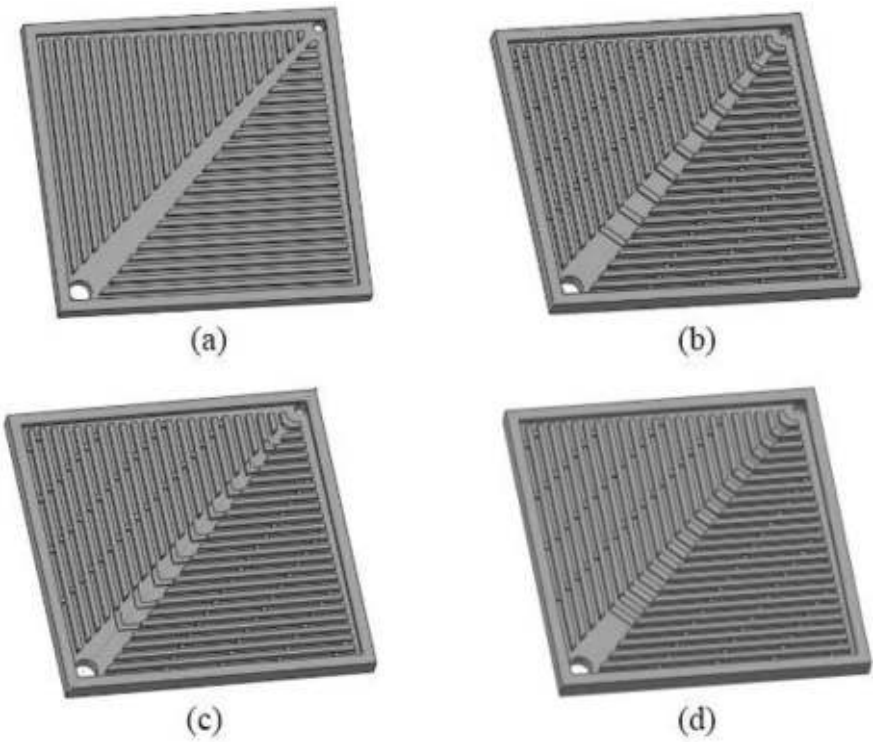

Fig. 1 – Baffle configuration on mother channels. (a) Model 1, (b) Model 2, (c) Model 3, and (d) Model 4.

$$R_a = \zeta_a j_a^{ref} \left(\frac{[H_2]}{[H_2]_{ref}}\right)^{\gamma_a} \left(e^{\frac{\alpha_a F \eta_a}{RT}} - e^{-\frac{\alpha_c F \eta_a}{RT}}\right) \quad (2)$$

$$R_c = \zeta_c j_c^{ref} \left(\frac{[O_2]}{[O_2]_{ref}}\right)^{\gamma_c} \left(-e^{\frac{\alpha_a F \eta_c}{RT}} + e^{-\frac{\alpha_c F \eta_c}{RT}}\right) \quad (3)$$

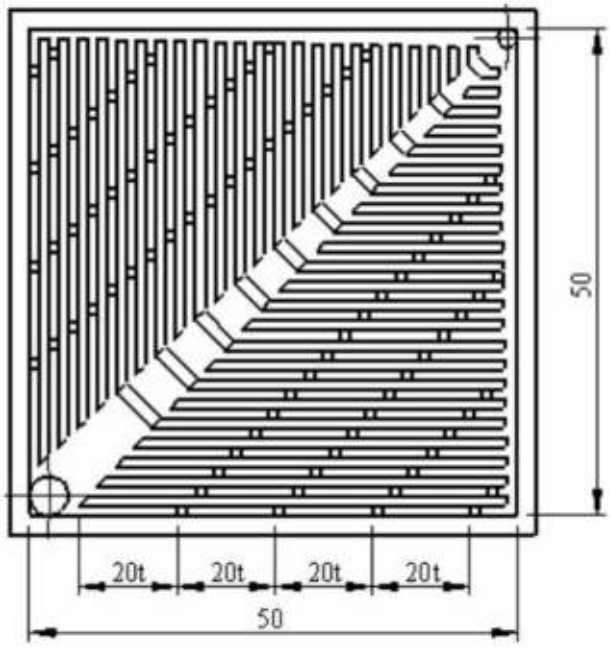

Fig. 2 – Baffle configuration on daughter channels.

Table 1 – Boundary condition and operation condition [18,28].

Property	Value	Unit
Catalyst layer porosity	0.4	
Gas diffusion layer porosity	0.6	
Open circuit voltage	1.05	V
Anode and cathode reference concentration	0.0008814	kmol/m^3
Anode and cathode charge transfer coefficient	1	
Anode reference current density	7.17	A/m^2. Pt
Cathode reference current density	7.17×10^5	A/m^2. Pt
Operation temperature	60	°C
Operation pressure	1	atm
Hydrogen mass flow	6.10^{-7}	Kg/s
Oxygen mass flow	2.10^{-5}	Kg/s

where ζ is the specific active surface area; j_a^{ref} and j_c^{ref} are, respectively, the anode and cathode reference exchange current density per active surface area; α_a and α_c are, respectively, the anode and cathode transfer coefficients; γ_a and γ_c are, respectively, the anode and cathode concentration exponents; η_a and η_c are, respectively, the overpotentials at the anode and cathode; and V_{oc} is the open-circuit voltage. Two transport equations regarding electron transportation through a solid material, Eq. (4), and proton transportation through a membrane, Eq. (5), were also coupled with the model.

$$\nabla.(\sigma_{sol} \nabla \varphi_{sol}) + R_{sol} = 0 \quad (4)$$

$$\nabla.(\sigma_{mem} \nabla \varphi_{mem}) + R_{mem} = 0 \quad (5)$$

where σ denotes the electron conductivity; φ, the electrical potential; and R, the volumetric transfer current, which is the

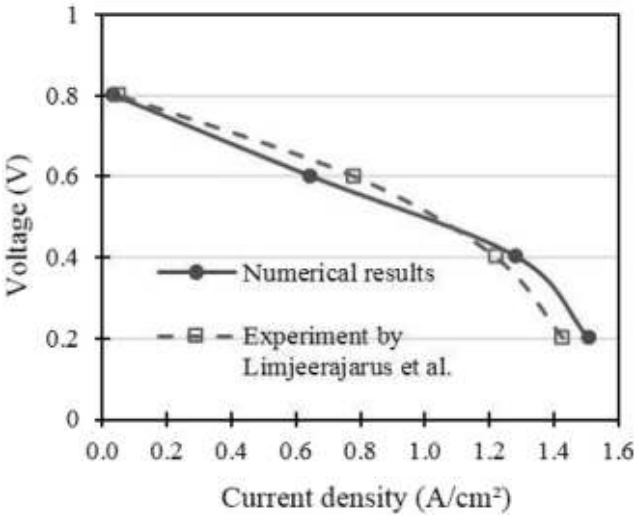

Fig. 3 – Comparison between the numerical results and experiments conducted by Limjeerajarus et al. [28].

source term in the catalyst layer equations, Eqs. (2) and (3). In these equations, $R_{sol} = -R_a$ when $R_a < 0$ and $R_{mem} = +R_a$ when $R_a > 0$. Furthermore, $R_{sol} = +R_{cat}$ when $R_{cat} > 0$ and $R_{mem} = -R_{cat}$ when $R_{cat} < 0$.

The driving force of the reaction is the activation overpotential on the surface (η), which is the difference between the potentials of the solid and membrane phases. The electric potential gain caused by the transportation from the anode jump to the cathode was evaluated by considering an open-circuit scenario with the open-circuit voltage, V_{oc}, on the cathode side; therefore, η was calculated using Eqs. (6) and (7) for the anode and cathode, respectively.

$$\eta_{an} = \varphi_{sol} - \varphi_{mem} \tag{6}$$

$$\eta_{cat} = \varphi_{sol} - \varphi_{mem} - V_{oc} \tag{7}$$

As long as the total electric current was generated at the cathode and anode, the current balance equation, Eq. (8), was valid:

$$\int R_{an} dV|_{anode} = \int R_{cat} dV|_{cathode} \tag{8}$$

Furthermore, the conductivity in the membrane was modeled by Eq. (9) [30].

$$\sigma_{mem} = \beta(0.514\lambda - 0.326)^{\omega} e^{1268\left(\frac{1}{303}-\frac{1}{T}\right)} \tag{9}$$

where $\beta = \omega = 1$ in the original correlation, and λ is the water content, which was computed using Eqs. (10) and (11) [30], considering the water activity, a, in Eq (12).

$$\lambda = 0.043 + 17.18a - 39.85a^2 + 36a^3 (a < 1) \tag{10}$$

$$\lambda = 14 + 1.4(a-1)\ (a > 1) \tag{11}$$

$$a = \frac{P_{wv}}{P_{sat}} + 2s \tag{12}$$

where s denotes the liquid water volume fraction. Moreover, the vapor pressure, P_{wv}, was computed based on the vapor molar fraction, x_{H_2O}, and local pressure, P, as presented in Eq. (13), and the saturated pressure was calculated in atm units using Eq. (14) [20].

$$P_{wv} = x_{H_2O}.P \tag{13}$$

$$log_{10}P_{sat} = -2.1794 + 0.02953(T - 273.17) - 9.1837x10^{-5}(T - 273.17)^2 + 1.4454x10^{-7}(T - 273.17)^3 \tag{14}$$

In addition, to determine the velocity uniformity, the uniformity index, γ, was calculated as presented in Eq. (15) based on the average velocity, $\bar{u}$, and the area, A [31].

$$\gamma = 1 - \int \frac{\sqrt{(\bar{u} - u)^2}}{2.A.\bar{u}} dA \tag{15}$$

Furthermore, the Sherwood number, Eq. (16), is a dimensionless quantity that can show the magnitude of mass convection compared with the diffusion. Assuming that the material and operating parameters are preserved, therefore, the diffusion is equivalent, and the Sherwood number increases with the mass transfer. As a result, this quantity can be used as a reference to evaluate the best design considering the mass transfer.

$$S_h = \frac{h_m D_h}{D_{i,j}} \tag{16}$$

where Dh denotes the hydraulic diameter; $D_{i,j}$, the binary diffusion coefficient; and h_m, the mass transfer convection coefficient, which can be calculated based on the mass flow of reactants that have already reacted, $\dot{m}$, and the generated electric current, A_{elec}, as indicated in Eq (17).

$$h_m = \frac{\dot{m}}{A_{elec}(C_o - C_s)} \tag{17}$$

Finally, the fuel cell net power of the fuel cell, W_{net}, was calculated using Eqs. (18) and (19) [24]:

$$W_{net} = W_{FC} - W_P \tag{18}$$

$$W_P = \Delta P.\frac{\dot{m}}{\rho} \tag{19}$$

where W_{FC} denotes the fuel cell gross power; W_P, the pump power used to supply the reactant; $\dot{m}$, the inlet reactant mass flow rate; ρ, the reactant density; and $\triangle P$, the pressure drop between the inlet and outlet of the channel.

Numerical methods and model validation

The model was imported into the Ansys–Fluent software which was used with the PEM fuel cell add-on module. A semi-implicit method was employed to solve the pressure-linked equation, and the SIMPLE algorithm was used in the solution method for the pressure-velocity coupling. Furthermore, a second-order discretization scheme was selected to guarantee the high accuracy of the solution. To improve the convergence rate, the multigrid cycle and the F-cycle were applied with the bi-conjugate gradient stabilized method (BCGSTAB), which was selected as the stabilization method for the equation of the species and anode–cathode potential. Due to the complex

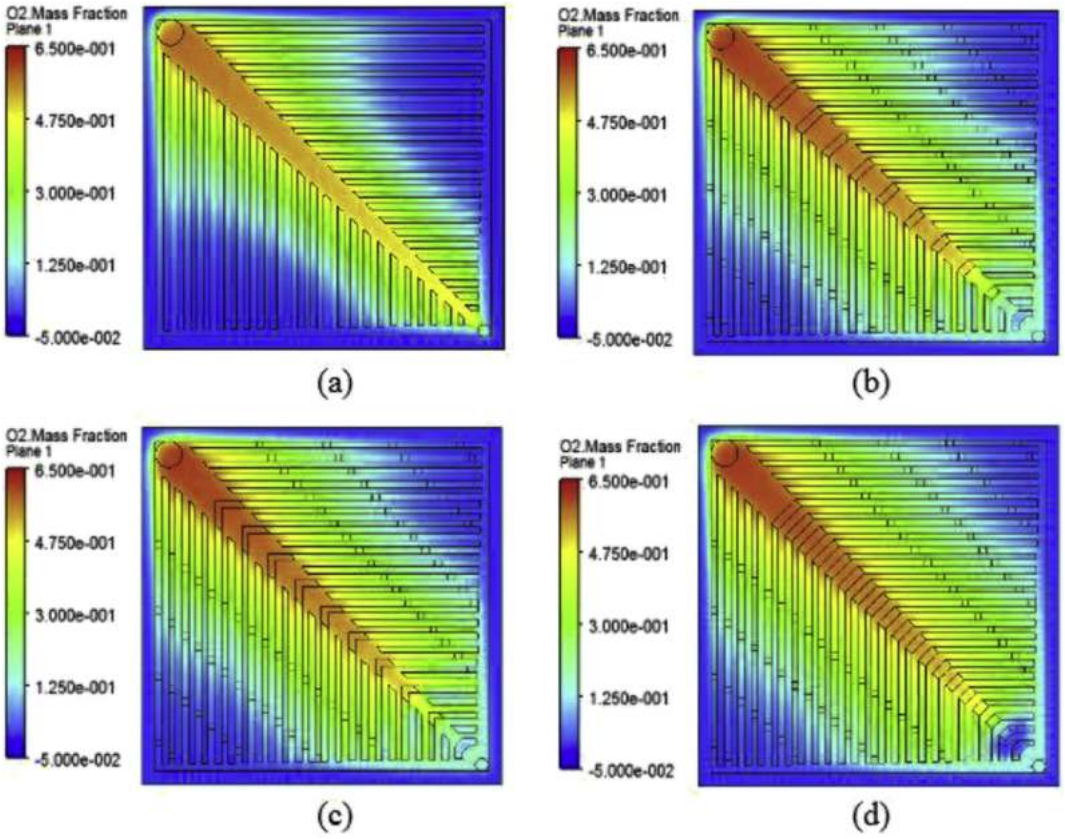

Fig. 4 – Distribution of oxygen mass fraction on the cathode side gas diffusion layer at 0.5 V. (a) Model 1, (b) Model 2, (c) Model 3, and (d) Model 4.

shape of the flow field, the Ansys meshing functionality was applied with a high smoothing value, and the element size of the mesh of the flow field was set to 0.0004 m, resulting in more accurate results as finer meshes lead to more precise results at each point. However, fine meshes also demand more computational power for the numerical calculations, increasing the time required to complete the simulation; therefore, experiments with different values of mesh fineness were conducted to determine the impact of the grid on the current density in order to identify a scenario in which the results were independent of the grid. Mesh fineness variations were set by changing the smoothing and relevance center of the mesh sizing. Optimal meshing was obtained when a difference in current density of less than 0.2% was achieved.

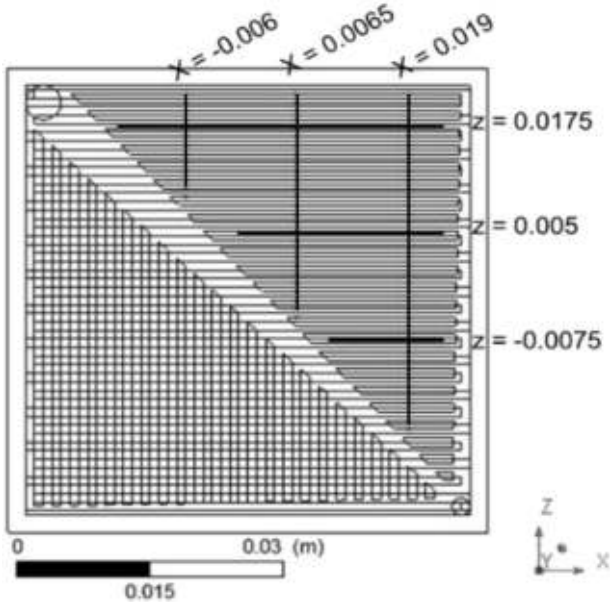

Fig. 5 – Position of the sample data of oxygen mass fractions in the cathode side gas diffusion layer.

Fig. 3 presents the comparison of the current density between the numerical results and experimental results conducted by Limjeerajarus et al. [28]. The parameters used in this numerical study were the same as those used by Limjeerajarus et al. [28]. Furthermore, the simulation results were similar to those obtained from the experiments.

Results and discussion

Fig. 4 presents the distribution of oxygen mass fraction for different flow field models on the cathode side gas diffusion layer at 0.5 V. The distribution of the oxygen mass fraction is more uniform in the flow field, in which the baffle was present, as the baffles in the mother channel force the flow of oxygen toward the branch channel. As a result, the flow of oxygen immediately directed to the outlet was reduced.

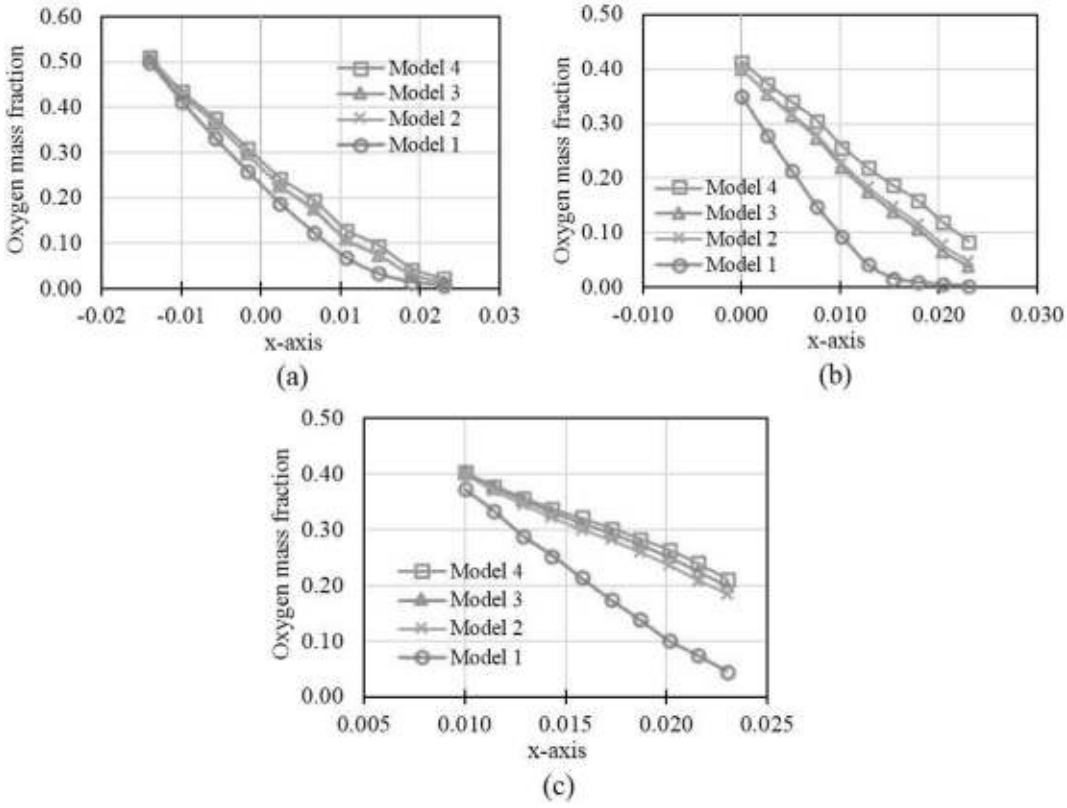

Fig. 6 – Oxygen mass fraction at sample points along the x-axis: (a) at z = 0.0195, (b) at z = 0.0057, and (c) at z = −0.0075.

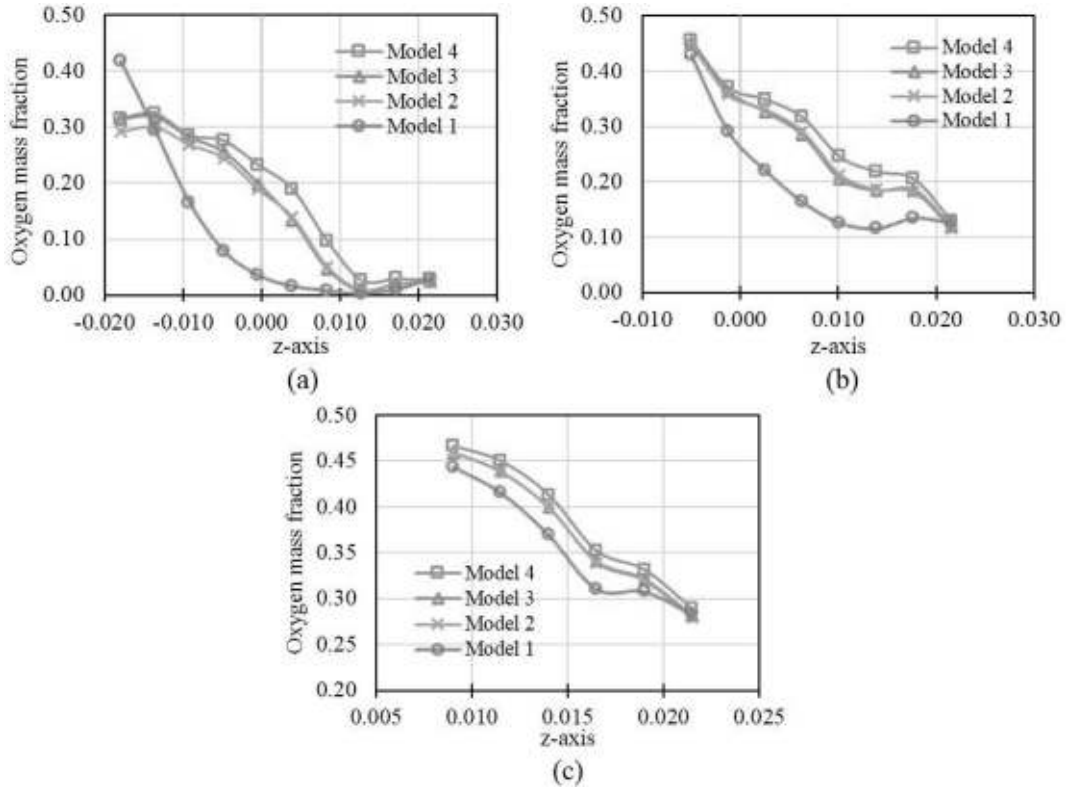

Fig. 7 – Oxygen mass fraction at sample points along the z-axis: (a) at x = 0.019, (b) at x = 0.0065, and (c) at x = −0.006.

Table 2 – Uniformity index and area-weight average.

Term	Model 1	Model 2	Model 3	Model 4
Uniformity Index Area-Wt.				
Velocity Magnitude	0.529	0.570	0.568	0.562
Static Pressure	0.912	0.902	0.904	0.896
Static Temperature	0.999	0.999	0.999	0.999
Mass fraction of O_2	0.649	0.739	0.737	0.761
Area-Weighted Average				
Current Flux Density Magnitude (A/m^2)	12371.44	14232.00	14183.88	14633.85
Power density (W/m^2)	4948.58	5692.80	5673.55	5853.54

Table 3 – Average oxygen concentration and Sherwood number.

Term	Model 1	Model 2	Model 3	Model 4	Unit
C_{in}	0.01858	0.01858	0.01858	0.01858	$kmol/m^3$
C_{out}	0.00595	0.00435	0.00443	0.00404	$kmol/m^3$
Co	0.00846	0.00960	0.00962	0.00999	$kmol/m^3$
Cs	0.00729	0.00844	0.00843	0.00886	$kmol/m^3$
Ci	0.00461	0.00553	0.00554	0.00592	$kmol/m^3$
Co–Cs	1.167	1.162	1.184	1.130	$kmol/m^3$
h_m	0.0275	0.0317	0.0310	0.0336	m/s
Sh	0.971	1.121	1.098	1.187	

The distribution obtained from model 2 was slightly better than that of model 3, as the square-shaped baffles could block the flow more efficiently. As a result, the flow directed to the branch channel increased, and sufficient supply to near the end of the branch channel was achieved. In model 4, which was a refinement of model 2, the increase in the number of baffles in the mother channel enabled the oxygen distribution to reach the end of the branch channel.

To quantitatively determine the distribution of the oxygen mass fraction at the cathode layer diffusion gas, measures were collected at different points along the line, parallel to the x- and z-axis, as presented in Fig. 5. These data can be seen in Figs. 6 and 7. Fig. 6 presents the measures of the mass fraction of oxygen on the lines parallel to the x-axis. As can be seen from Fig. 5, the lowest oxygen mass fraction value along the x-axis parallel lines occurred with model 1 (without baffles), whereas the highest mass fraction value occurred in flow fields with tight baffles (model 4). Meanwhile, the mass fraction distributions between models 2 and 3 were not significantly different.

Fig. 7 presents the distribution of oxygen mass fraction in the gas diffusion layer of the cathode side along several lines in parallel to the z-axis. As can be seen from Fig. 7(a) and (b), the addition of baffles increased the oxygen content in the branch channel, near the inlet and middle channels. The branch channel near the inlet was the longest; therefore, it required more oxygen, as the percentage of the total flow directed to the branches increased with the resistance in the mother channel. Meanwhile, in the regional branch channel near the outlet in Fig. 7(c), the oxygen mass fraction of model 4 was still higher than that of the other models, as the input mass flow was sufficient, considering the area of the geometry. Furthermore, in model 1 (without baffles), a high flow rate of air was directed to the outlet.

Table 2 indicates that the oxygen mass fraction is directly proportional to the current and power densities. Moreover, the uniformity of the oxygen mass fraction positively impacts the generated current and power densities [8,32]. Model 4 produced the highest uniformity for the oxygen mass fraction (0.761), resulting in an increase of 18.29% in the current density when compared with model 1. The uniformity of flow velocity was not always directly proportional to the uniformity of the mass fraction due to the longer channels, such as the branch channel near the inlet, which demanded a higher flow rate, because at each distance, they are consumed for the reaction. Meanwhile, the pressure and velocity parameters have similar trends.

Table 3 presents the average oxygen concentration of each model, considering the same value of input oxygen concentration. As a result, the concentration obtained from model 4 was the highest in the flow field (Co), on the surface of the gas diffusion layer (Cs), and the surface of the catalyst (Ci). In addition, the mass transfer coefficient (h_m) and Sherwood number (Sh) in model 4 were significantly higher (approximately 22.25%) when compared with model 1, as the Co–Cs difference in model 4 was relatively low. This low difference between Co and Cs could be due to the flow properties in model 4, as the supply of oxygen was uniform and sufficient; therefore, the oxygen supply to the gas diffusion layer was higher than the amount of oxygen that reacted. Contrarily, higher oxygen concentrations occurred in the flow field of

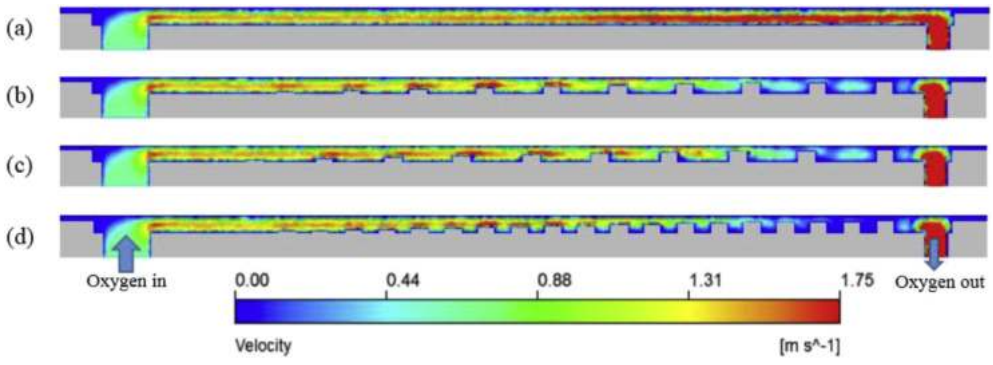

Fig. 8 – Velocity distribution in the diagonal cross section of the mother channel with a variety of flow field designs. a) Model 1, b) Model 2, c) Model 3, and d) Model 4.

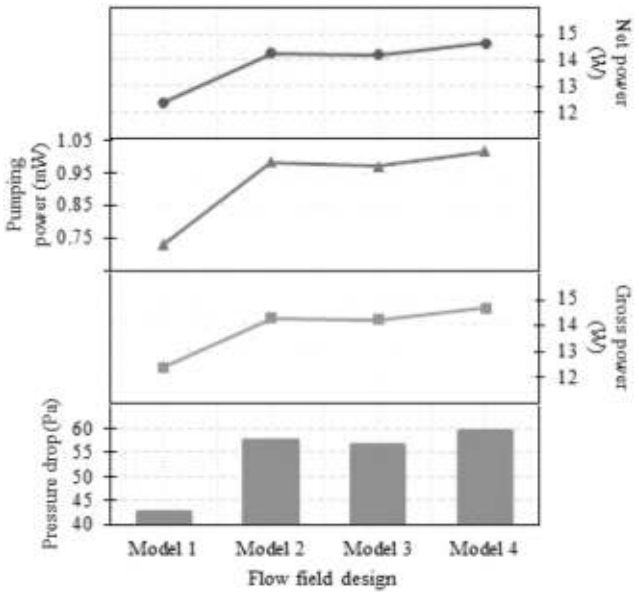

Fig. 9 – Impacts of flow field design on the pressure drop, gross power, pumping power, and net power.

model 3 when compared with model 2 (Table 3); however, the current density of model 3 was lower (Table 2). One possible explanation of this discrepancy is the better uniformity of oxygen mass fraction in model 2. Furthermore, the rectangular-shaped baffle led to a greater pressure toward GDL, increasing the average oxygen concentration in GDL when compared with that of model 3.

Fig. 8 indicates that the use of baffles on the mother channel increased the flow resistance, thus increasing the flow of reactants into the branch channel and filling the areas with lower concentrations of the reactant. Furthermore, the blockage efficiency of the baffles on the mother channel increased with the number of baffles and the reduction of their distance, increasing the flow rate of the reactant to the outlet. Moreover, the use of baffles increased the flow velocity at the top of the baffles, forcing the reactants to flow toward the GDL and CL. Meanwhile, in model 1 (without baffles), the flow velocity is in the middle of the channel; therefore, the flow rate toward the GDL was reduced, and the flow rate directed to the outlet was increased.

The addition of baffles to the flow field significantly increased the pressure drop. Fig. 9 indicates that in flow fields with baffles (models 2–4), a substantial pressure drop occurred when compared with model 1 (without baffles). A large pressure drop results in the requirement of more pump power, therefore reducing the net power generated. However, the pressure drop on a single stack was relatively small due to the small reactant flow mass required. As a result, the pump power needed was also relatively very small compared with the electric power generated; therefore, the net power generated was not significantly affected. The pressure drop in model 4, in which the baffles were close to each other, was 39.07% greater than that of model 1 (without baffles); however, the pump power required was only 0.007% of the gross power produced.

Conclusion

The addition of baffles to the leaf-shaped flow field increased the current density and power density of PEM fuel cells up to 18.29%. The addition of baffles in the mother channel combined with an appropriate configuration inhibited the flow of air to the outlet, increasing the uniformity of the oxygen mass fraction. As a result, a more assured supply of reactants was provided at each reaction location, increasing the generated electric current.

Declaration of competing interest

The authors declare that they have no known competing financial interests or personal relationships that could have appeared to influence the work reported in this paper.

Acknowledgments

The authors grateful to Lembaga Pengelola Dana Pendidikan (LPDP) Ministry of Finance of Republic of Indonesia for a doctoral scholarship to A'rasy Fahruddin. Also facility support from the Department of Mechanical Engineering and Direktorat Riset dan Pengabdian kepada Masyarakat (DRPM), Institut Teknologi Sepuluh Nopember (ITS) Indonesia, are greatly acknowledged.

REFERENCES

[1] Wu H. A review of recent development: transport and performance modeling of PEM fuel cells. Appl Energy 2016;165:81–106. https://doi.org/10.1016/j.apenergy.2015.12.075.
[2] Haile SM. Fuel cell materials and components. Acta Mater 2003;51:5981–6000. https://doi.org/10.1016/j.actamat.2003.08.004.
[3] Thomas CE. Fuel cell and battery electric vehicles compared. Int J Hydrogen Energy 2009;34:6005–20.
[4] Wang Y, Fournier J. Rule-based energy management strategy of a lithium-ion battery, supercapacitor and PEM fuel cell system. Energy Procedia 2019;158:2555–60. https://doi.org/10.1016/j.egypro.2019.02.003.
[5] Shiva Kumar S, Himabindu V. Hydrogen production by PEM water electrolysis – a review. Mater Sci Energy Technol 2019;2:442–54. https://doi.org/10.1016/j.mset.2019.03.002.
[6] Wang Y, Mishler J, Adroher XC. A review of polymer electrolyte membrane fuel cells: technology, applications, and needs on fundamental research. Appl Energy 2011;88:981–1007. https://doi.org/10.1016/j.apenergy.2010.09.030.
[7] Badduri SR, Srinivasulu GN, Rao SS. Influence of bio-inspired flow channel designs on the performance of a PEM fuel cell. Chin J Chem Eng 2019. https://doi.org/10.1016/j.cjche.2019.07.010. Pre proof.
[8] Manso AP, Marzo FF, Barranco J, Garikano X, Garmendia Mujika M. Influence of geometric parameters of the flow fields on the performance of a PEM fuel cell. A review. Int J Hydrogen Energy 2012;37:15256–87. https://doi.org/10.1016/j.ijhydene.2012.07.076.

[9] Li X, Sabir I. Review of bipolar plates in PEM fuel cells: flow-field designs. Int J Hydrogen Energy 2005;30:359–71. https://doi.org/10.1016/j.ijhydene.2004.09.019.
[10] Dhahad HA, Alawee WH, Hassan AK. Experimental study of the effect of flow field design to PEM fuel cells performance. Renew Energy Focus 2019;30:71–7. https://doi.org/10.1016/j.ref.2019.05.002.
[11] Lim BH, Majlan EH, Daud WRW, Rosli MI, Husaini T. Numerical analysis of modified parallel flow field designs for fuel cells. Int J Hydrogen Energy 2017;42:9210–8. https://doi.org/10.1016/j.ijhydene.2016.03.189.
[12] Watkins DS, Dircks KW, Epp DG. Fuel cell fluid flow field plate. US Patent No. 5.108.849. 1992.
[13] Liu H, Li P, Wang K. Optimization of PEM fuel cell flow channel dimensions d Mathematic modeling analysis and experimental verification. Int J Hydrogen Energy 2013;38:9835–46. https://doi.org/10.1016/j.ijhydene.2013.05.159.
[14] Roshandel R, Arbabi F, Moghaddam GK. Simulation of an innovative flow-field design based on a bio inspired pattern for PEM fuel cells. Renew Energy 2012;41:86–95. https://doi.org/10.1016/j.renene.2011.10.008.
[15] Kloess JP, Wang X, Liu J, Shi Z, Guessous L. Investigation of bio-inspired flow channel designs for bipolar plates in proton exchange membrane fuel cells. J Power Sources 2009;188:132–40. https://doi.org/10.1016/j.jpowsour.2008.11.123.
[16] Guo N, Leu MC, Koylu UO. Bio-inspired flow field designs for polymer electrolyte membrane fuel cells. Int J Hydrogen Energy 2014;39:21185–95. https://doi.org/10.1016/j.ijhydene.2014.10.069.
[17] Ozden A, Ercelik M, Ouellette D, Colpan CO, Ganjehsarabi H, Hamdullahpur F. Designing, modeling and performance investigation of bio-inspired flow field based DMFCs. Int J Hydrogen Energy 2017;42:21546–58. https://doi.org/10.1016/j.ijhydene.2017.01.007.
[18] Fahruddin A, Ichsani D, Taufany F, Kukuh Widodo BU. The effect of channel width on biometric flow field towards performance of polymer electrolyte membrane fuel cell. J Eng Sci Technol 2019;14:2552–64.
[19] Fahruddin A, Ichsani D, Taufany F, Widodo BUK. The effect of mother channel width on biometric flow field towards polymer electrolyte membrane fuel cell performance. J Phys Conf Ser 2019:1402. https://doi.org/10.1088/1742-6596/1402/4/044042.
[20] Heidary H, Kermani MJ, Prasad AK, Advani SG, Dabir B. Numerical modelling of in-line and staggered blockages in parallel flowfield channels of PEM fuel cells. Int J Hydrogen Energy 2017;42:2265–77. https://doi.org/10.1016/j.ijhydene.2016.10.076.
[21] Heidary H, Kermani MJ, Dabir B. Influences of bipolar plate channel blockages on PEM fuel cell performances. Energy Convers Manag 2016;124:51–60. https://doi.org/10.1016/j.enconman.2016.06.043.
[22] Ghanbarian A, Kermani MJ. Enhancement of PEM fuel cell performance by flow channel indentation. Energy Convers Manag 2016;110:356–66. https://doi.org/10.1016/j.enconman.2015.12.036.
[23] Yin Y, Wang X, Shangguan X, Zhang J, Qin Y. Numerical investigation on the characteristics of mass transport and performance of PEMFC with baffle plates installed in the flow channel. Int J Hydrogen Energy 2018;43:8048–62. https://doi.org/10.1016/j.ijhydene.2018.03.037.
[24] Yin Y, Wang X, Zhang J, Shangguan X, Qin Y. Influence of sloping baffle plates on the mass transport and performance of PEMFC. Int J Energy Res 2019;43:2643–55. https://doi.org/10.1002/er.4306.
[25] Thitakamol V, Therdthianwong A, Therdthianwong S. Mid-baffle interdigitated flow fields for proton exchange membrane fuel cells. Int J Hydrogen Energy 2011;36:3614–22. https://doi.org/10.1016/j.ijhydene.2010.12.060.
[26] Heidary H, Kermani MJ, Advani SG, Prasad AK. Experimental investigation of in-line and staggered blockages in parallel flowfield channels of PEM fuel cells. Int J Hydrogen Energy 2016;41:6885–93. https://doi.org/10.1016/j.ijhydene.2016.03.028.
[27] Chen T, Xiao Y, Chen T. The impact on PEMFC of bionic flow field with a different branch. Energy Procedia 2012:134–9. https://doi.org/10.1016/j.egypro.2012.08.047.
[28] Limjeerajarus N, Charoen-Amornkitt P. Effect of different flow field designs and number of channels on performance of a small PEFC. Int J Hydrogen Energy 2015;40:7144–58. https://doi.org/10.1016/j.ijhydene.2015.04.007.
[29] ANSYS, Inc. ANSYS FLUENT fuel cell modules manual. Canonsburg, PA: ANSYS, Inc.; 2013.
[30] Springer TE. Polymer electrolyte fuel cell model. J Electrochem Soc 1991;138:2334–42. https://doi.org/10.1149/1.2085971.
[31] Nassau Christopher J, Agarwal Ramesh K. Curvature effects and flow uniformity optimization of a blood microchannel. Mech Eng Mater Sci Indep Study 2018;71.
[32] Hossain MS, Shabani B, Cheung CP. Enhanced gas flow uniformity across parallel channel cathode flow field of Proton Exchange Membrane fuel cells. Int J Hydrogen Energy 2016;42:5272–83. https://doi.org/10.1016/j.ijhydene.2016.11.042.